Biomaterials Research

RESEARCH ARTICLE

Open Access

Construction of magnetic nanochains to achieve magnetic energy coupling in scaffold

Cijun Shuai[1,2], Xuan Chen[1], Chongxian He[2], Guowen Qian[1], Yang Shuai[3], Shuping Peng[4,5,6], Youwen Deng[7*] and Wenjing Yang[1*]

Abstract

Background: Fe_3O_4 nanoparticles are highly desired for constructing endogenous magnetic microenvironment in scaffold to accelerate bone regeneration due to their superior magnetism. However, their random arrangement easily leads to mutual consumption of magnetic poles, thereby weakening the magnetic stimulation effect.

Methods: In this study, magnetic nanochains are synthesized by magnetic-field-guided interface co-assembly of Fe_3O_4 nanoparticles. In detail, multiple Fe_3O_4 nanoparticles are aligned along the direction of magnetic force lines and are connected in series to form nanochain structures under an external magnetic field. Subsequently, the nanochain structures are covered and fixed by depositing a thin layer of silica (SiO_2), and consequently forming linear magnetic nanochains (Fe_3O_4@SiO_2). The Fe_3O_4@SiO_2 nanochains are then incorporated into poly l-lactic acid (PLLA) scaffold prepared by selective laser sintering technology.

Results: The results show that the Fe_3O_4@SiO_2 nanochains with unique core–shell structure are successfully constructed. Meanwhile, the orderly assembly of nanoparticles in the Fe_3O_4@SiO_2 nanochains enable to form magnetic energy coupling and obtain a highly magnetic micro-field. The in vitro tests indicate that the PLLA/Fe_3O_4@SiO_2 scaffolds exhibit superior capacity in enhancing cell activity, improving osteogenesis-related gene expressions, and inducing cell mineralization compared with PLLA and PLLA/Fe_3O_4 scaffolds.

Conclusion: In short, the Fe_3O_4@SiO_2 nanochains endow scaffolds with good magnetism and cytocompatibility, which have great potential in accelerating bone repair.

Keywords: Magnetic microenvironment, Fe_3O_4 nanoparticles, Magnetic nanochains, Magnetic energy coupling, Bone scaffold

Introduction

Recent scaffolds lack the capacity to effectively modulate cell growth or tissue reconstruction, resulting in slow bone regeneration and even failure of bone implantation [1–4]. It is well known that cells are magnetically sensitive due to the diamagnetism of cell membranes [5], and exposure to magnetic fields served to alter membrane flux and regulate ion channels and biochemical pathways [6, 7]. In this case, a series of cell behaviors will be mediated. Inspired by this, it is significant to construct an endogenous magnetic microenvironment in bone scaffold to mediate cell behaviors and tissue regeneration via magnetic stimulation.

As a typical magnetic material, Fe_3O_4 nanoparticles have been widely used in tissue engineering field due to their superior magnetic properties and good biocompatibility [8]. In addition, Fe_3O_4 nanoparticles enable to decompose into oxygen and iron in the body and can be easily removed from the body after degradation by

*Correspondence: drywdeng@csu.edu.cn; yangwenjing@jxust.edu.cn

[1] Institute of Additive Manufacturing, Jiangxi University of Science and Technology, Nanchang 330013, China
[7] Department of Spine Surgery, Third Xiangya Hospital, Central South University, Changsha 410013, China
Full list of author information is available at the end of the article

oxygen transport and metabolism [9]. In our previous study [10], the introduction of Fe_3O_4 nanoparticles into bone scaffolds constructed an endogenous magnetic microenvironment that enhanced cell activity and accelerated new bone generation. It is worth noting that the random arrangement of Fe_3O_4 nanoparticles in scaffold easily leads to mutual repulsive of magnetic poles between adjacent nanoparticles, thereby weakening the magnetic strength. In this case, the scaffold cannot fully exert its regulation on cell behaviors.

The directional assembly of Fe_3O_4 nanoparticles into ordered nanochain structures is expected to solve the above problem. Under an external magnetic field, the internal magnetic dipole moment of Fe_3O_4 nanoparticles enable to be rapidly deflected to the direction of magnetic field [11, 12]. Moreover, the attractive magnetic dipole interaction will drive multiple Fe_3O_4 nanoparticles to assemble into ordered magnetic nanochain structures along with magnetic force lines [13, 14]. Compared with randomly arranged Fe_3O_4 nanoparticles, the magnetic nanochain structures can realize the magnetic energy coupling between the nanoparticles, thereby enhancing the magnetic strength [15–17]. Li et al. synthesized uniform linear cobalt nanochains with a coating layer of polyvinylpyrrolidone under an external magnetic field [18]. Wan et al. synthesized magnetic nanochains and fixated with a protective mesoporous silicon shell for osteoclast-targeted inhibition and heterogeneous nanocatalysis [19].

In this study, Fe_3O_4@SiO_2 magnetic nanochains with core–shell structure were synthesized utilizing magnetic-field-guided interface co-assembly of nanoparticles. In short, Fe_3O_4 nanoparticles were firstly coated with a layer of protective SiO_2 film. Then, the above products were aligned and assembled into nanochains under an external magnetic field. Thereafter, the nanochains were fixated by further deposition of SiO_2 shell to permanently preserve their structure. Then, the Fe_3O_4@SiO_2 nanochains were loaded into PLLA and prepared into porous PLLA/Fe_3O_4@SiO_2 scaffold using selective laser sintering (SLS). The microscopic morphology, chemical composition, and physicochemical properties of Fe_3O_4@SiO_2 were analyzed. The cell activity, osteogenic differentiation and mineralization abilities induced by the PLLA/Fe_3O_4@SiO_2 scaffold were investigated and analyzed in detail. Moreover, the osteogenesis-related gene expressions of runt-related transcription factor-2 (Runx2), osteopontin (OPN), osteocalcin (OCN) and osterix (OSX) in cells co-cultured with the scaffold were assessed.

Experimental sections

Materials

Medical-grade PLLA powders were obtained from Shenzhen Polymtek Biomate-rial Co., Ltd. (Shenzhen, China). Fe_3O_4 nanoparticles with an average diameter of 100 nm, tetraothorsilicate (TEOS), sodium citrate dihydrate ($C_6H_5Na_3O_7{\cdot}2H_2O$), sodium hydroxide (NaOH) and concentrated ammonia solution ($NH_3{\cdot}H_2O$, 28 wt.%) were purchased from Aladdin Chemistry Co. Ltd. (Shanghai, China). The above chemicals were applied as received without further purification.

Synthesis of one-dimensional Fe3O4@SiO2 nanochains

The Fe_3O_4@SiO_2 nanochains were prepared through the magnetic-field-guided interface co-assembly of Fe_3O_4 nanoparticles, as shown in Fig. 1. First, 20 mg of Fe3O4 nanoparticles was dispersed in 60 mL ethanol-aqueous solution by ultrasonication for 20 min. Subsequently, 5 mL of ammonia solution (28 wt.%) was dropped into the resulting solution with mechanical agitating (800 rpm) for 30 min. Then, the agitating speed was reduced to 300 rpm, and 10 mL of ethanol solution with TEOS ($V_{ethanol}$:V_{TEOS} = 9:1) were dropped in the solution to coat Fe_3O_4 nanoparticles with a layer of protective SiO_2 film in the early stage of the sol–gel reaction of TEOS. After reaction for 15 min, the above solution was exposed in a static magnetic field (55 mT-65 mT) for 2 min to induce the linear arrangement of Fe_3O_4 nanoparticles without stirring, forming numerous nanochain structures. After standing for another 10 min, the nanochain structures were further fixated with an addition SiO_2 shell. Finally, the fixated core–shell Fe_3O_4@SiO_2 magnetic nanochains were magnetically separated from the suspension, washed three times with ethanol and distilled water and dried in a vacuum oven.

Preparation of scaffolds

For comparison, PLLA, PLLA/Fe_3O_4 and PLLA/Fe_3O_4@SiO_2 scaffolds were respectively fabricated. Prior to fabricating, PLLA/Fe_3O_4@SiO_2 and PLLA/Fe_3O_4 powders were prepared as follows. 4.6 g of PLLA powders and 0.4 g of Fe_3O_4@SiO_2 nanochains or Fe_3O_4 nanoparticles were added to a beaker containing 30 mL of ethanol, in which the feeding mass ratio of Fe_3O_4@SiO_2 or Fe_3O_4 to PLLA was effectively controlled at 8 wt.%. Then, the suspension was ultrasound for 30 min, following by vigorously stirring 1 h. Thereafter, the result suspensions were vacuum dried for 24 h at 65 °C, obtaining PLLA/Fe_3O_4@SiO_2 or PLLA/Fe_3O_4 powders.

The representative PLLA/Fe_3O_4@SiO_2 scaffold with honeycomb structure was fabricated via SLS technology. In detail, the PLLA/Fe_3O_4@SiO_2 powders were paved on the powder bed and selectively laser scanned according to the designed three-dimensional model, with laser power at 2.5 W, scanning speed at 100 mm/s and scanning distance at 0.24 mm [20, 21]. The modeling platform

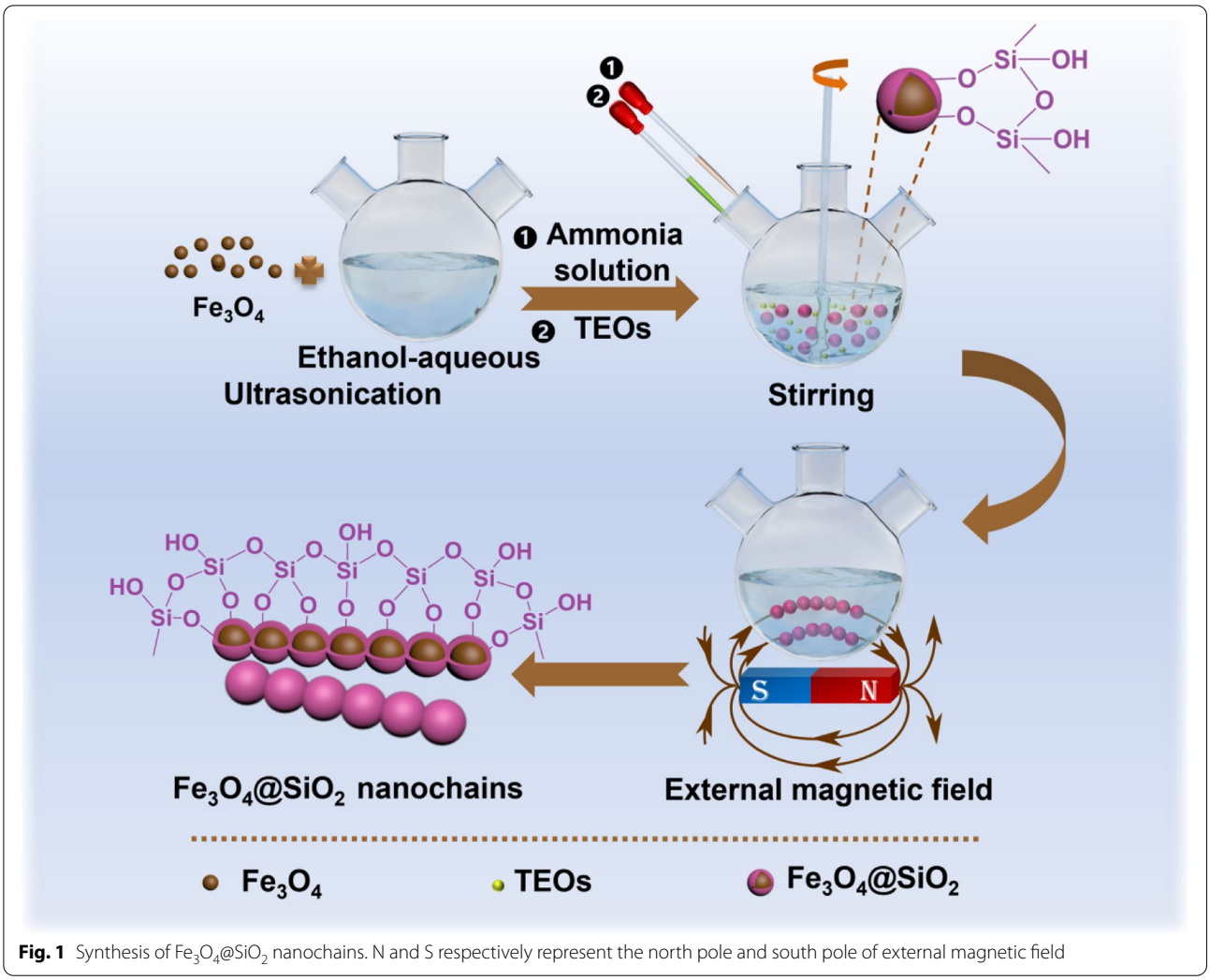

Fig. 1 Synthesis of Fe_3O_4@SiO_2 nanochains. N and S respectively represent the north pole and south pole of external magnetic field

gradually descended with each layer of powders was sintered until the scaffold was completely formed.

Measurement and characterization

The morphologies of the Fe_3O_4@SiO_2 nanochains were observed by transmission electron microscope (TEM, TALOS F200X, USA). The chemical structure, compositions and crystal structures of the Fe_3O_4@SiO_2 or/and Fe_3O_4 powders were detected by X-ray photoelectron spectrometer (XPS, EscaLab 250Xi, USA), Fourier transform infra-red spectrometer (FTIR, FTIR 850, China) and X-ray diffractometer (XRD, D/MAX-RA, Japan). The magnetic properties of Fe_3O_4@SiO_2 and Fe_3O_4 powders were evaluated using a vibrating sample magnetometer (VSM, LakeShore7404, USA). The mechanical properties were detected on a universal testing machine, with samples ($6 \times 5 \times 3$ mm^3) for the compressive tests and dumbbell samples ($L_0 = 10.1$ mm, $h = 2.2$ mm) for the tensile tests. The thermal behaviors of scaffolds were tested by a Pyris 1 thermal gravimetric analyzer (TGA, PerkinElmer, USA) under nitrogen at a heating rate of 20 °C/min. Water contact angle on PLLA, PLLA/Fe_3O_4 and PLLA/Fe_3O_4@SiO_2 scaffolds were assessed using an optical contact angle meter (DM-501, Japan).

Cytocompatibility

The PLLA, PLLA/Fe_3O_4, PLLA/Fe_3O_4@SiO_2 scaffolds (ϕ 8×2 mm^3) were sterilized by immersing in 70% ethanol solution for 2 h and irradiating with UV for 12 h. Then, the sterilized scaffolds were individually placed in 48-well culture plates. MG-63 cells (Sigma, Shanghai, China) were selected to investigate the cytocompatibility of scaffolds. MG-63 cells cultured in Dulbecco's Modified Eagle's Medium (DMEM) were washed with D-Hanks solution three times and were digested with trypsin. The resulting solution were centrifuged at 1000 r/min for 5 min. The cell suspension was diluted to 8×10^3 cells/

mL. All the cells were incubated in a humidified condition with 5% CO_2 at 37 °C.

The cells at a density of 4×10^3 cells/well were incubated on the surface of sterilized scaffolds in 48-well plates containing DMEM, in which the DMEM was updated daily. After incubating for 3 and 7 days, each cell-scaffold sample was washed with PBS three times, and then immersed in 5% glutaraldehyde for 30 min to fix cells. Thereafter, the cell-scaffold samples were dehydrated with 30%, 50%, 70%, 80%, 90%, 95% and absolute ethyl alcohol in sequence and dried for 12 h at room temperature. After coated with gold, the cell morphology on each scaffold was observed by scanning electron microscope (SEM).

Cell viabilities on the scaffolds were studied by a live/dead staining kit (Beyotime, China). At the specified time (3 and 7 days), the culture medium was removed, and the cells were detached from scaffolds and rinsed using PBS three times. Subsequently, the cells were stained with 2 μM Calcein-AM for 30 min at 37 °C. Finally, the stained cells were visualized using a fluorescence microscope (Olympus, Japan).

Cell proliferation was quantitatively assessed using Cell Counting Kit-8 (CCK-8, Beyotime, China) assay. The cell-scaffold samples were harvested from culture medium after 1, 4 and 7 days of cultivating. Then, the samples were washed with PBS and transferred into 96-well plates containing 100 μL CCK-8 reagent. After incubating for 2 h, the absorbance of the solution was detected utilizing a microplate reader (Thermal, USA) at 450 nm. Each group was carried out three parallel experiments.

The alkaline phosphatase (ALP) activity of the cells on scaffolds was determined to assess the osteogenic differentiation. After incubating for 7 days, the harvested cells from samples were washed with PBS 3 times and fixed with 4% paraformaldehyde for 15 min. Then, ALP staining kit (Beyotime, China) was dropped to stain the cells, and the stained cells were monitored using an inverted microscope (TE2000U, Japan).

The mineralization nodules of MG-63 cells cocultured with scaffolds were qualitatively investigated using Alizarin Red staining. The cells were seeded on scaffolds in 6-well plates for 7 days at a density of 1×10^4 cells/mL. After that, the cell-scaffold samples were fixed using 4% paraformaldehyde and rinsed with PBS. Subsequently, the samples were stained with 0.04 M Alizarin Red for 10 min. After rinsing, the samples were observed under a light microscope.

Scaffold-mediated cell differentiation and osteogenesis were further studied. For this, the expression of several relative genes containing runt-related transcription factor-2 (Runx2), osteopontin (OPN), osteocalcin (OCN) and osterix (OSX) were detected with quantitative real-time polymerase chain reactions (RT-PCR). After incubating for 3 and 7 days, the RNA isolation of cells was employed using TRIzox reagent, and then the RNA was reverse transcribed to cDNA using PrimeScript 1st strand cDNA synthesis kit. Finally, the levels of Runx2, OPN, OCN and OSX were calculated using the $2^{-\Delta\Delta Ct}$ method. Each sample was analyzed three times.

Statistical analysis

All data were conducted by Student's *t*-test for independent samples and presented as means ± standard deviation, where $^{**}p < 0.01$ and $^{*}p < 0.05$ represented significant difference.

Results

Fe3O4@SiO2 nanochains

The representative one-dimensional structure of the Fe_3O_4@SiO_2 nanochains were observed using TEM. As shown in Fig. 2a and b, the Fe_3O_4@SiO_2 nanochains presented a unique core–shell structure, in which Fe_3O_4 nanoparticles served as cores with a diameter of about 100 nm and SiO_2 layers served as shells with a thickness of about 25 nm. Based on Fast Fourier transform (FFT, Fig. 2c and d), the interplanar distance between adjacent lattice fringes was 0.25 nm, which was in great agreement with the (311) lattice planes of Fe_3O_4. Moreover, the diffraction rings depicted in the selected area electron diffraction (SAED) patterns respectively corresponded to the (220), (311), (400), (440) and (422) lattice planes of cubic Fe_3O_4 (Fig. 2e). The Si, Fe and O elements were clearly exhibited in the elemental mapping images (Fig. 2f-i). Particularly, the distribution of Si and Fe elements further confirmed the shell-core structure of the nanochains. The results confirmed that the Fe_3O_4 nanoparticles could be induced to align in a nanochain though magnetic dipolar interaction under external magnetic field.

Magnetic field distribution around single Fe_3O_4 nanoparticle and nanochain in the same direction of external magnetic field was analyzed using finite element method (COMSOL Multiphysics), as shown in Fig. 3a-c. It could be seen that the magnetic dipole moment of a Fe_3O_4 nanoparticle reached a saturated value under the adequately strong magnetic field (Fig. 3a). When the centerlines of two adjacent nanoparticles were aligned with the direction of the external magnetic field, the dipole–dipole interaction was attractive (Fig. 3b). In the case of the interaction energy was large enough to overcome thermal fluctuations, the magnetic dipole–dipole force drove the self-assembly of nanoparticles into nanochain along the dipole moment (Fig. 3c). In this condition, the dipole–dipole coupling reached the maximum, and the magnetism of nanochain could be regarded as the

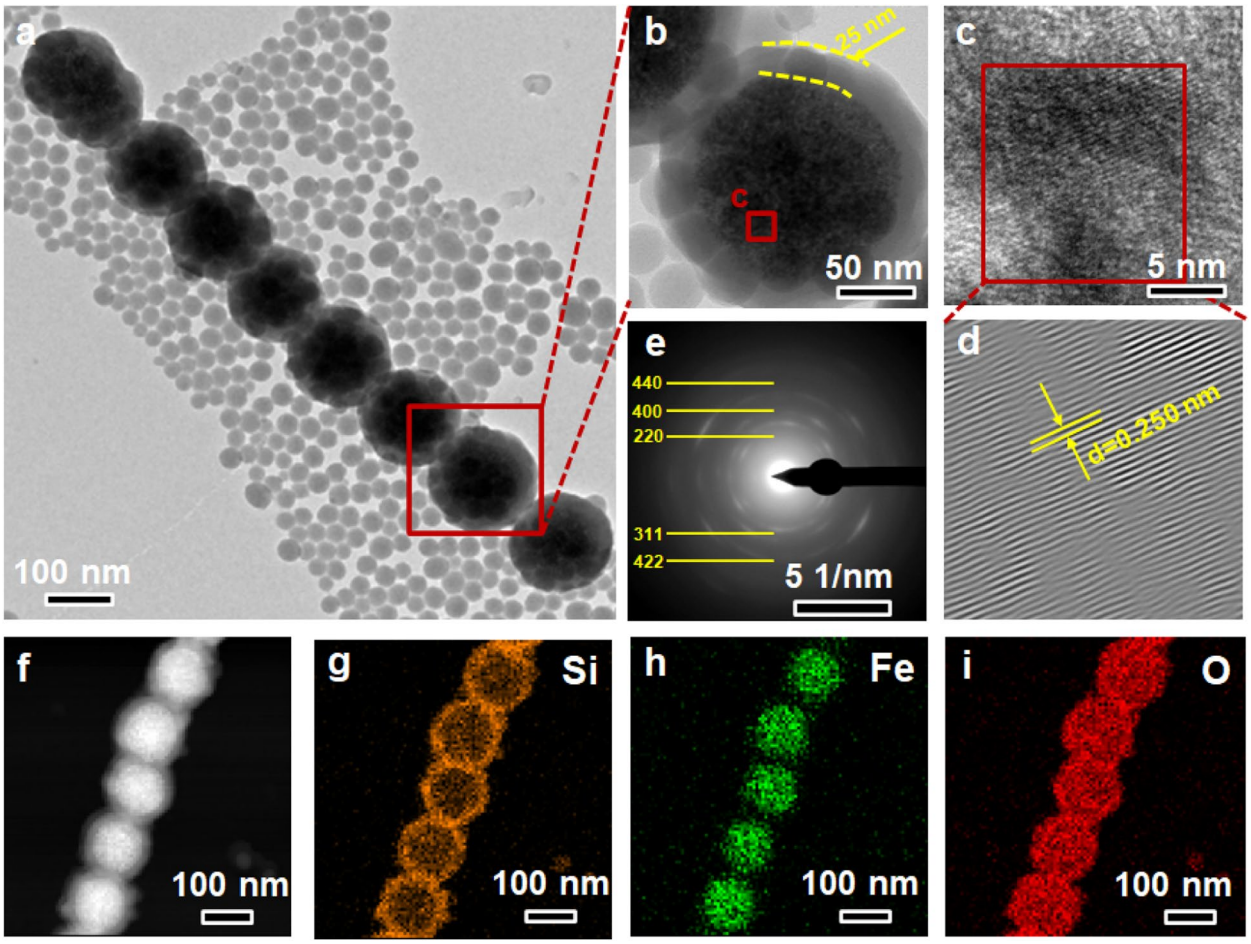

Fig. 2 **a-c** TEM images, (**d**) the inverse-FFT image, (**e**) SAED patterns and (**f-i**) element mapping images of Fe_3O_4@SiO_2 nanochains

magnetic energy coupling among multiple nanoparticles. The magnetic strength of nanochain was higher than that of randomly arranged Fe_3O_4 nanoparticles.

The magnetic properties of Fe_3O_4 nanoparticles and Fe_3O_4@SiO_2 nanochains were detected and presented in Fig. 3d. It could be seen that both nanoparticles and nanochains exhibited superior magnetism, which was an important advantage for their applicability in biomedicine [22, 23]. The saturation magnetization of Fe_3O_4 was 52.2 emu/g. The relatively low saturation magnetization of Fe_3O_4@SiO_2 was due to the introduction of non-magnetic SiO_2 shells decreased the weight ratio of Fe_3O_4 in Fe_3O_4@SiO_2. This phenomenon was also discovered by M. Tarhini and A. Bitar et al. [24, 25].

XPS spectra of Fe_3O_4@SiO_2 nanochains were presented in Fig. 3e. The typical Fe2p, O1s and Si2p peaks were clearly observed (Fig. 3 e1). In detail, the peaks centered at 711.4, 723.0 and 726.0 eV were respectively corresponded to $Fe^{2+}2p_{3/2}$, $Fe^{2+}2p_{1/2}$ and $Fe^{3+}2p_{1/2}$ of Fe_3O_4 (Fig. 3 e2), while the peaks centered at 102.7 and 104.2 eV were assigned to Si–OH and Si–O-Si of SiO_2 (Fig. 3 e3) [26]. It was worth noting that the binding energy of O1s was 533.1 eV (Fig. 3 e4), which was higher than that of Fe_3O_4 (529.6 eV) by 3.5 eV. This was mainly due to the formation of Fe–O-Si chemical bond (530.2 eV) decreased the electronic density of O binding Fe, resulting in the chemical shift of binding energy of O1s. Moreover, the coexistence of Si–O-Si and Fe–O-Si verified the coating of SiO_2 on the nanochains.

The XRD patterns of Fe_3O_4 nanoparticles and Fe_3O_4@SiO_2 nanochains were exhibited in Fig. 3f. There were typical diffraction peaks of (200), (311), (400), (422), (511) and (440) planes, which corresponded to Fe_3O_4 presented in both patterns, confirming that the crystal structure of Fe_3O_4 nanoparticles were completely preserved during the synthesis of Fe_3O_4@SiO_2. Compared with Fe_3O_4, a new broad diffraction at around 20° appeared in Fe_3O_4@SiO_2, which was attributed to the amorphous SiO_2 shell [27]. In the FTIR spectrum (Fig. 3g), the absorption peak at 1076 cm^{-1} in Fe_3O_4@SiO_2 was adscripted to Si–O

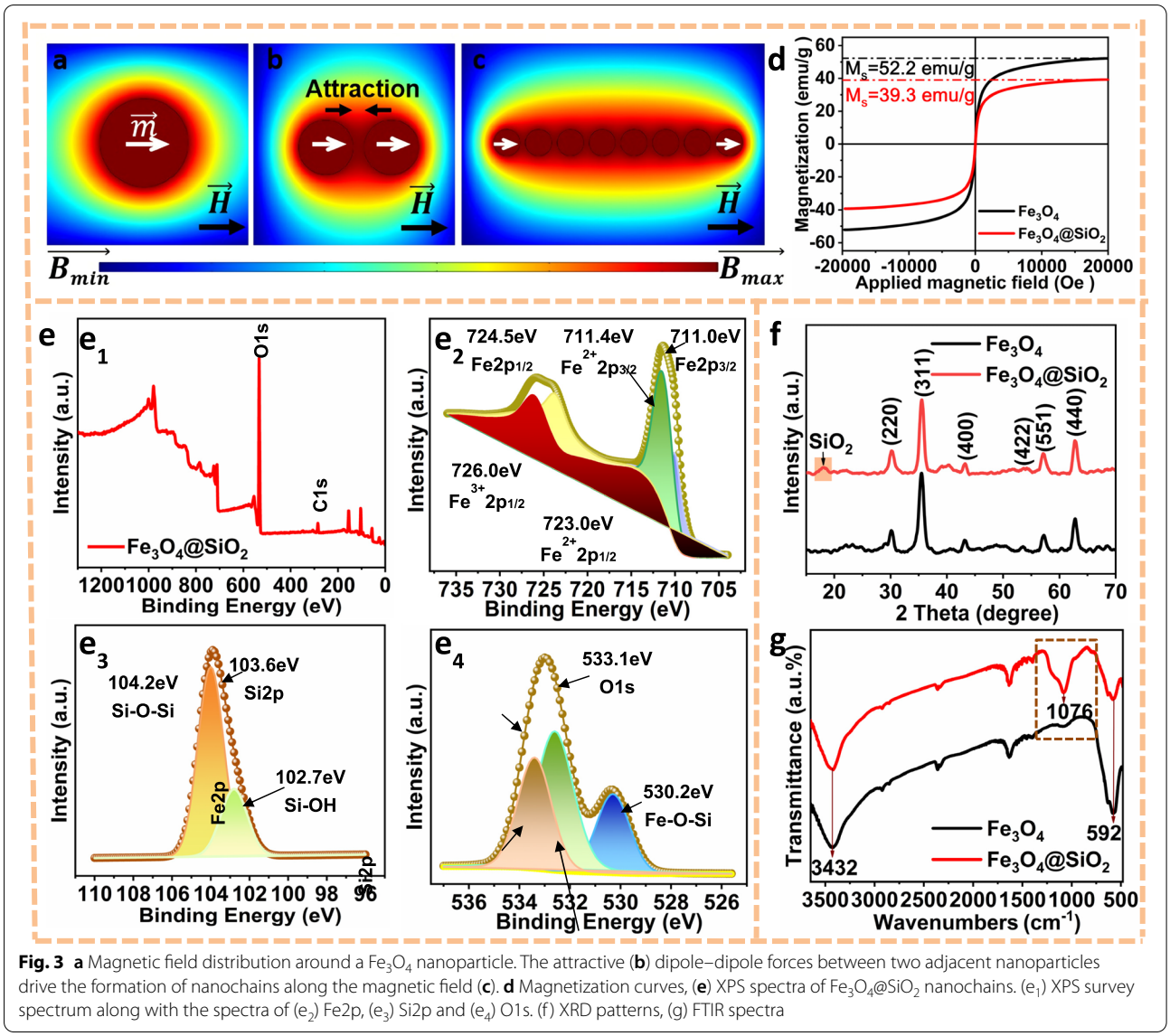

Fig. 3 **a** Magnetic field distribution around a Fe_3O_4 nanoparticle. The attractive (**b**) dipole–dipole forces between two adjacent nanoparticles drive the formation of nanochains along the magnetic field (**c**). **d** Magnetization curves, (**e**) XPS spectra of Fe_3O_4@SiO_2 nanochains. (e_1) XPS survey spectrum along with the spectra of (e_2) Fe2p, (e_3) Si2p and (e_4) O1s. (f) XRD patterns, (g) FTIR spectra

bond while the peak at 592 cm^{-1} was attributed to Fe–O bond [28–30], which further confirmed that the core–shell structure of Fe_3O_4@SiO_2 nanochains.

Physical and chemical properties

The porous scaffold with honeycomb structure was shown in Fig. 4a. The pore size of the scaffold was 800 ± 50 μm, which was proven to be beneficial to cell adhesion and climbing growth [31, 32]. The phase composition of the scaffolds was assessed using XRD (Fig. 4b). It can be clearly observed that the diffraction peaks belonged to (010), (110), (203) and (205) planes of PLLA [33]. By contrast, the new diffraction peaks corresponding to (311), (400), (551) and (440) crystal planes confirmed the spinel structure of Fe_3O_4 in PLLA/Fe_3O_4 and PLLA/Fe_3O_4@SiO_2 scaffolds [34].

The magnetic behaviors of the PLLA, PLLA/Fe_3O_4 and PLLA/Fe_3O_4@SiO_2 scaffolds were shown in Fig. 4c and d. It was clearly seen that the introduction of Fe_3O_4 and Fe_3O_4@SiO_2 endowed the non-magnetic PLLA scaffold favorable magnetic properties. This was conducive to construct magnetic microenvironment in scaffold, which was expected to enhance cell viability and promote cell growth through magnetic stimulation.

Mechanical properties of the scaffolds were evaluated via compressive and tensile tests, with the results shown in Fig. 4e and f. The compressive strength and modulus of PLLA scaffolds were only 22.3 ± 0.9 MPa and 78.4 ± 6.2 MPa. Encouragingly, the compressive

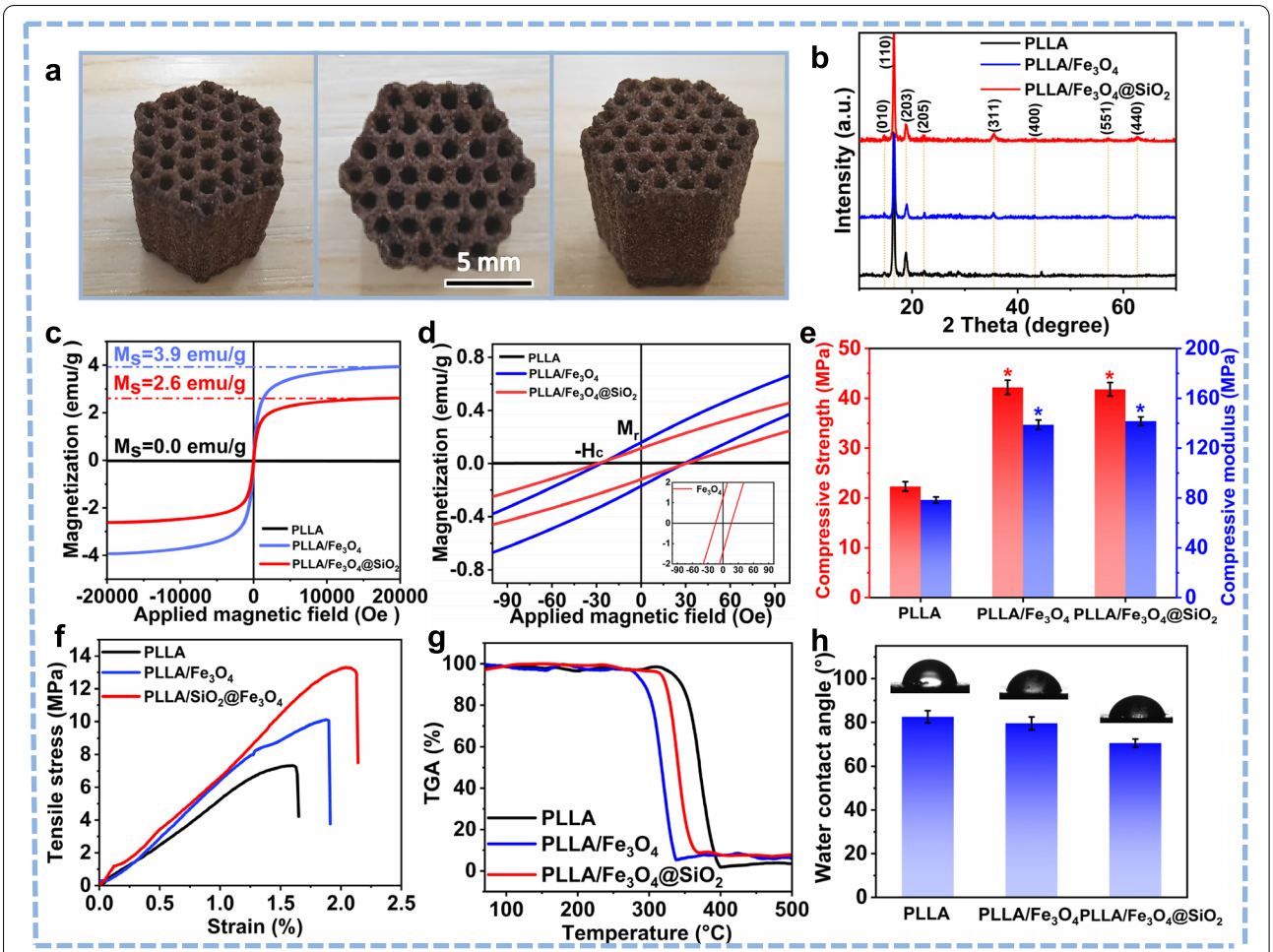

Fig. 4 **a** Optical graphs of SLS prepared honeycomb scaffold. **b** XRD patterns. **c** Magnetization curves. **d** Magnetization behaviors at magnetic field from -90 to 90 Oe. **e** Compressive strength and compressive modulus (n = 5, *$p < 0.05$), (**f**) tensile stress–strain curves, (**g**) TGA curves and (**h**) hydrophilicity of PLLA, PLLA/Fe_3O_4 and PLLA/Fe_3O_4@SiO_2 scaffolds

strength and modulus of the PLLA/Fe_3O_4@SiO_2 scaffolds were 41.8 ± 1.6 MPa and 142.6 ± 8.5 MPa, which were increased by 87.4% and 80.6% compared with PLLA scaffolds. Moreover, the PLLA/Fe_3O_4@SiO_2 scaffolds also exhibited much higher the tensile strength and strain than those of PLLA and PLLA/Fe_3O_4 scaffolds, which were 13.34 ± 1.2 MPa and 2.13%, respectively. The high mechanical properties of PLLA/Fe_3O_4@SiO_2 scaffolds were attributed to that the Fe_3O_4@SiO_2 nanochains acted as rigid reinforcement to enhance the stress transfer efficiency in the matrix.

The TGA measurement were performed to analyze the thermal decomposition and the corresponding residual weight of scaffolds (Fig. 4g). The slight weight loss below 300 °C of the scaffolds was related to the evaporation of adsorbed water molecules. Obviously, the thermal decomposition temperature of PLLA scaffolds was about 300 ~ 400 °C, while the range of decomposition temperature leftward shifted and narrowed after adding Fe_3O_4 and Fe_3O_4@SiO_2. This confirmed that the addition of Fe_3O_4 and Fe_3O_4@SiO_2 catalyzed the thermal decomposition of PLLA. Additionally, the residual weight of the PLLA/Fe_3O_4 and PLLA/Fe_3O_4@SiO_2 scaffolds was 7.4 wt.% and 7.6 wt.%, respectively, which was close to the nominal content (8 wt.%) of Fe_3O_4 and Fe_3O_4@SiO_2 introduced into PLLA matrix.

Generally, a scaffold with favorable hydrophilicity is more conducive to cell adhesion [35]. The hydrophilicity of PLLA, PLLA/Fe_3O_4 and PLLA/Fe_3O_4@SiO_2 scaffolds was investigated via water contact angle test. As shown in Fig. 4h, the contact angle on the PLLA scaffold was 86.2 ± 2.8°. By contrast, the contact angle decreased after the adding Fe_3O_4 nanoparticles, indicating the improvement of hydrophilicity. This could be attributed to the presence of hydroxyl groups on the Fe_3O_4 nanoparticles in aqueous environment. Moreover, the PLLA/Fe_3O_4@

SiO_2 scaffolds exhibited the best hydrophilicity, which was mainly due to the silanol groups of SiO_2 absorbed water molecule via hydrogen bonding.

Cytocompatibility

The cytocompatibility of scaffolds is a necessary and crucial element in the bone repair process because it determines whether cells can adhere, grow, and proliferate on the scaffold [36, 37]. Herein, the cytocompatibility of the PLLA, PLLA/Fe_3O_4 and PLLA/Fe_3O_4@SiO_2 scaffolds were assessed. As shown in Fig. 5a, cells adhered well on all scaffolds, indicating that the PLLA, PLLA/Fe_3O_4 and PLLA/Fe_3O_4@SiO_2 scaffolds had good biocompatibility. Particularly, better cell adhesion morphology displayed on PLLA/Fe_3O_4@SiO_2 scaffold than that on PLLA and PLLA/Fe_3O_4 scaffolds at the same time point. Moreover, the cells completely expanded and essentially presented normal topological configuration on PLLA/Fe_3O_4@SiO_2 scaffold after 7 days of cultivation, indicating that the Fe_3O_4@SiO_2 nanochains in scaffold were more conducive to cell adhesion and expansion.

Cell viability is also an important indicator for evaluating the cytocompatibility of the scaffold [38]. To investigate the cells viability induced by the PLLA, PLLA/Fe_3O_4 and PLLA/Fe_3O_4@SiO_2 scaffolds, the cells were strained with calcein AM. Normally, calcein AM only stains living cells, because calcein AM as a dye can be transformed into a membrane impermeable fluorescent analogue by the cell esterases, and the fluorescence will leak out when the cell membrane is completely damaged [39, 40].

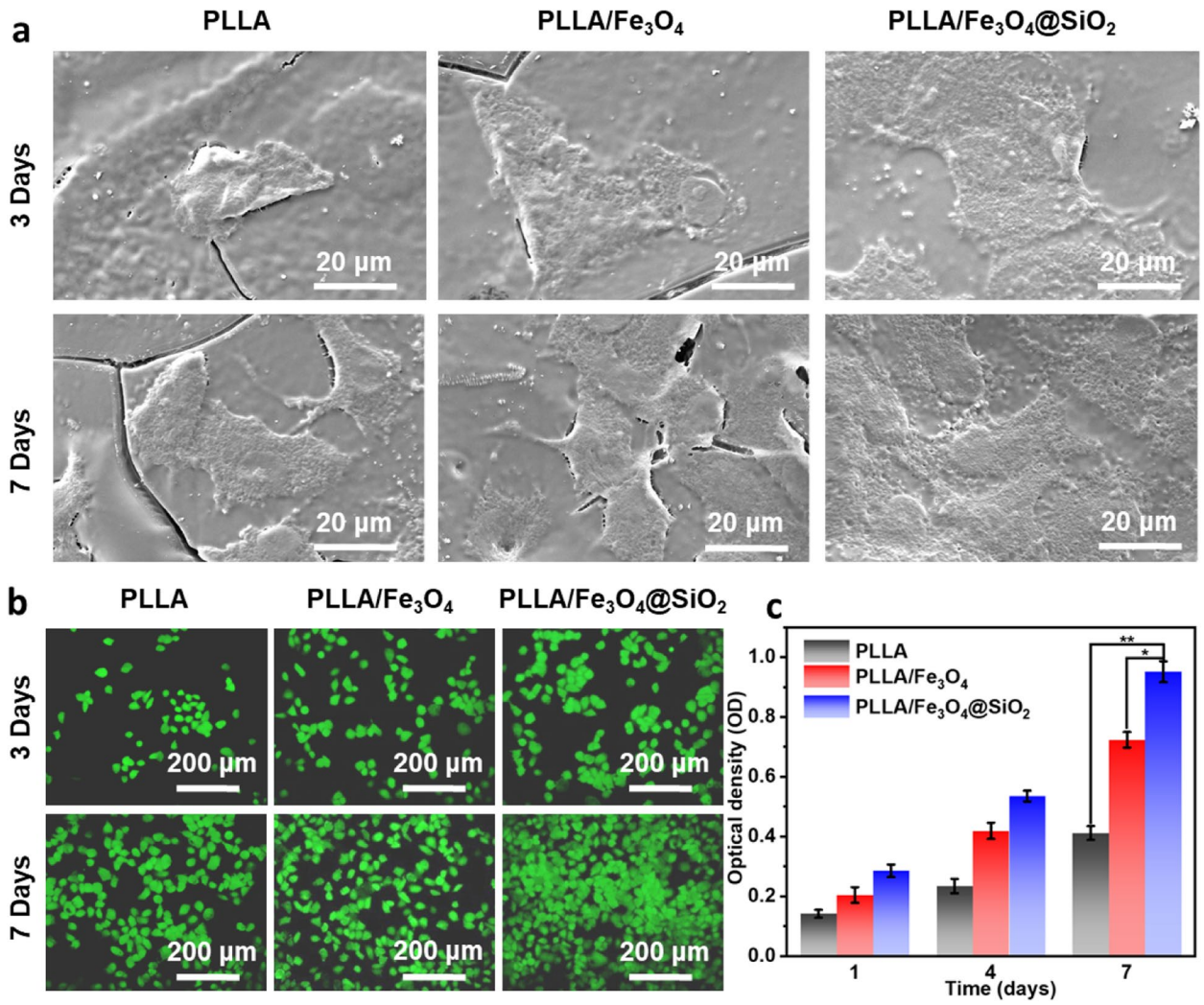

Fig. 5 **a** Adhesion morphologies of MG-63 cells on PLLA, PLLA/Fe_3O_4 and PLLA/Fe_3O_4@SiO_2 scaffolds. **b** Fluorescence images of cells cultured after 3 and 7 days on the scaffolds. **c** Cell proliferation on the scaffolds (n = 5, $^*p < 0.05$, $^{**}p < 0.01$)

As shown in Fig. 5b, the density of living cells in PLLA, PLLA/Fe_3O_4 and PLLA/Fe_3O_4@SiO_2 scaffold groups was significantly enhanced with time, confirming that all scaffolds possessed the ability to enhance cell activity. Notably, the cells increased exponentially from 3 to 7 days with the highest density observing in the cells which cocultured with PLLA/Fe_3O_4@SiO_2 scaffold, indicating that the Fe_3O_4@SiO_2 nanochains in scaffold significantly enhanced cell viability and promoted cell proliferation.

Cell proliferation is one of the important physiological functions of living cells. To quantitatively study the cell proliferation capacity on the PLLA, PLLA/Fe_3O_4 and PLLA/Fe_3O_4@SiO_2 scaffolds, the CCK-8 assay was carried out (Fig. 5c). It could be clearly seen that the optical density (OD) value of cells on all the scaffolds increased significantly with incubating time. Compared with the PLLA scaffold, higher OD value of cells presented on the PLLA/Fe_3O_4 scaffold, indicating that the Fe_3O_4 nanoparticles in the scaffold promoted cell proliferation. Especially, the OD value of cells on PLLA/Fe_3O_4@SiO_2 scaffold was markedly higher than that on PLLA/Fe_3O_4 scaffold, indicating that the Fe_3O_4@SiO_2 nanochains further promoted cell proliferation.

As one of the early indicators of osteogenic differentiation [41], ALP activity of cells cultured on the scaffolds for 7 days was qualitatively analyzed (Fig. 6a). It could be clearly seen that the cells cocultured with the PLLA/Fe_3O_4@SiO_2 scaffold samples exhibited higher ALP activity than PLLA and PLLA/Fe_3O_4 samples. As one of the late markers of osteogenic differentiation [42], the Alizarin Red staining was performed to assess the extracellular matrix mineralization of cells cocultured with the scaffolds for 7 days (Fig. 6b). As expected, there were obvious red precipitates in all scaffold groups. It was worth noting that the mineral deposition was significantly enhanced in PLLA/Fe_3O_4@SiO_2 samples compared to other groups, mainly due to the stronger magnetic stimulation effect of Fe_3O_4@SiO_2 nanochains. The above results demonstrated that the Fe_3O_4@SiO_2 nanochains in scaffold markedly enhanced cell activity and promoted cell proliferation, differentiation, and mineralization.

The bone-related gene expressions including RUNX2, OPN, OCN and OSX on PLLA, PLLA/Fe_3O_4 and PLLA/Fe_3O_4@SiO_2 scaffolds were investigated (Fig. 7). From an overall perspective, the expression levels of RUNX2, OPN, OCN and OSX on day 7 were greatly higher than on day 3. Especially, the expression level of them on the PLLA/Fe_3O_4@SiO_2 scaffold were markedly higher than that on PLLA/Fe_3O_4 and PLLA scaffolds at any time. The results showed that the Fe_3O_4@SiO_2 nanochains provided a more favorable magnetic microenvironment for cell differentiation than Fe_3O_4 nanoparticles in scaffolds, confirming that the superior capability of Fe_3O_4@SiO_2 nanochains to promote cell differentiation.

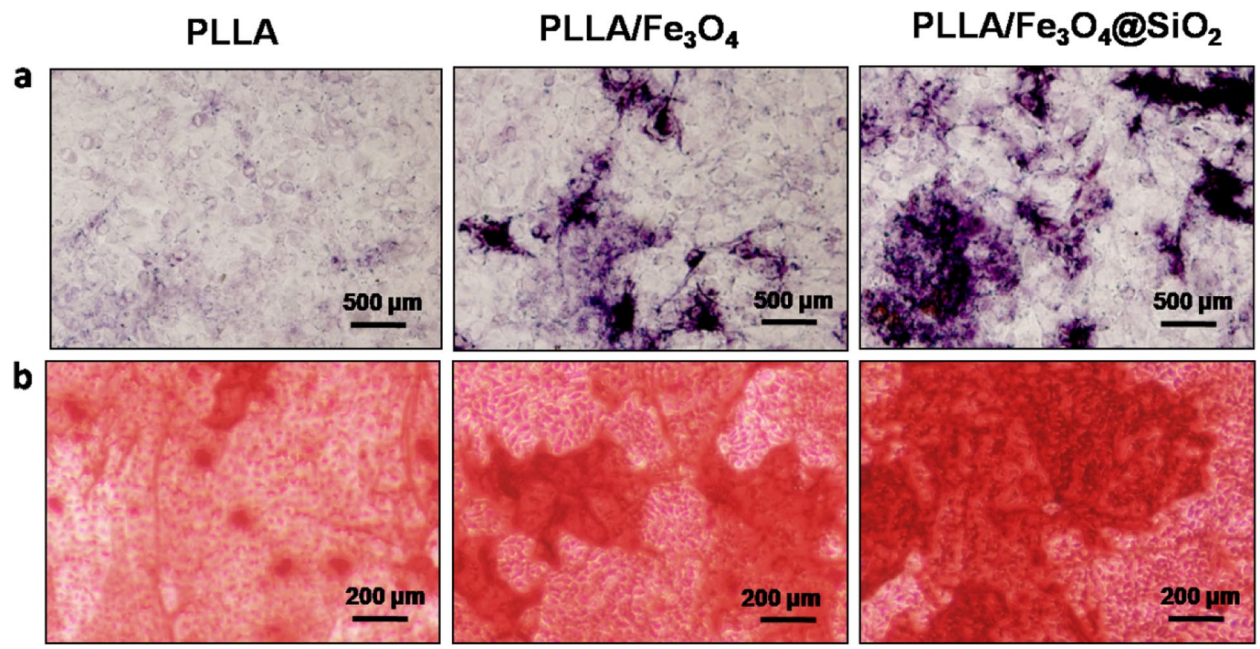

Fig. 6 **a** The ALP and (**b**) Alizarin Red staining of cells on PLLA, PLLA/Fe_3O_4 and PLLA/Fe_3O_4@SiO_2 scaffolds after 7 days of cultivation

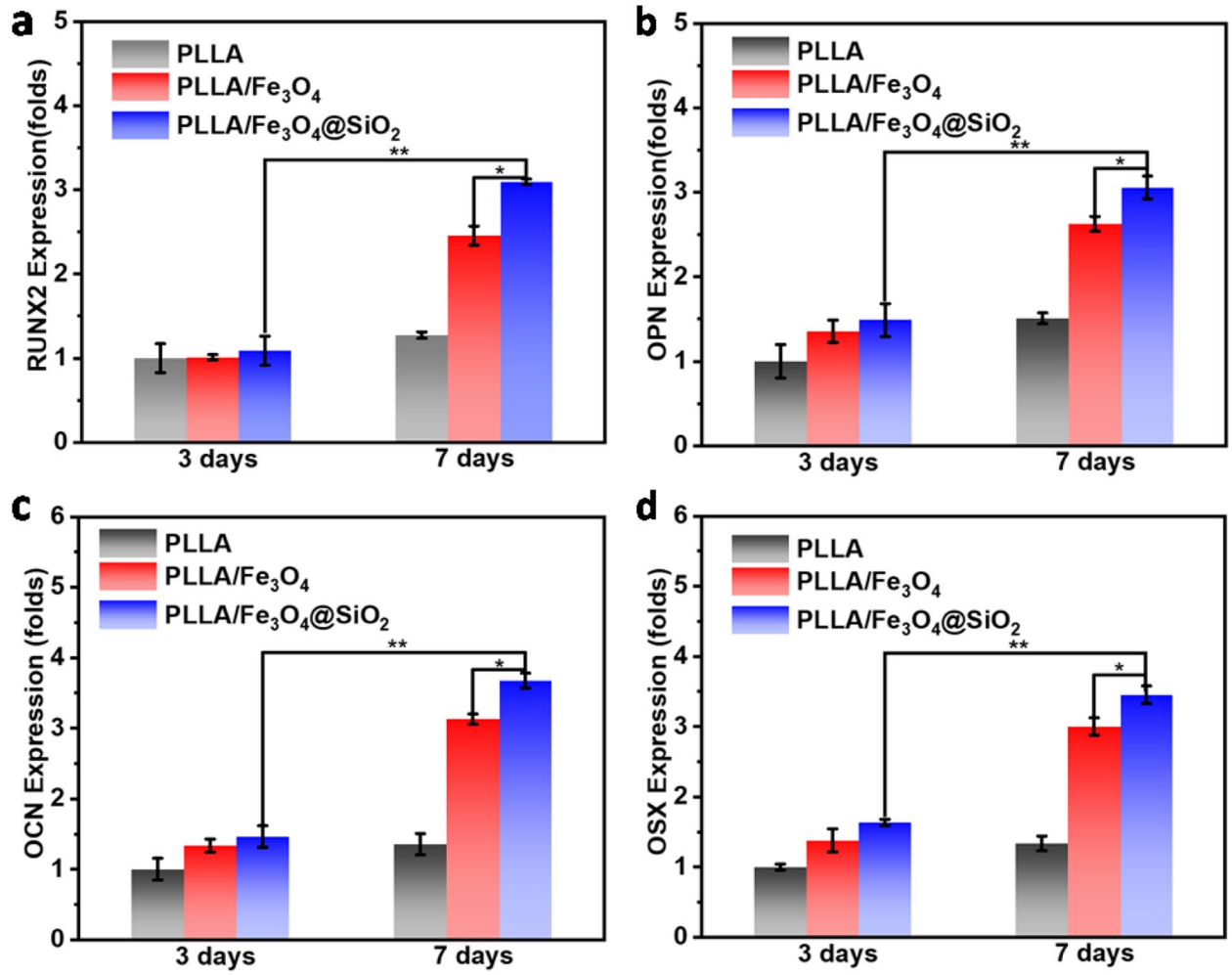

Fig. 7 The expressions of (**a**) RUNX2, (**b**) OPN, (**c**) OCN and (**d**) OSX on the scaffolds after 3 and 7 days of culture (n = 5, *$p < 0.05$, **$p < 0.01$)

Discussion

It is well known that various cells, such as mesenchymal stem cells, osteoblasts, and endothelial cells are magnetically sensitive due to the diamagnetism of cell membranes [43]. Inspired by these, researchers have applied different external magnetic fields to study the roles of magnetic stimulation in bone repair in recent years [44, 45]. It was found that the external magnetic fields could induce a series of cell behaviors by regulating cell surface receptors and signaling pathways via magnetic stimulations, thereby accelerating new bone regeneration or inhibiting osteoclast resorption. However, the need of magnetic field generators limits the clinical application of magnetic stimulation to a certain extent.

To solve the above problem, it would be an effective means to construct an endogenous magnetic microenvironment in bone scaffolds by introducing magnetic materials. As a highly biocompatible and magnetic materials, Fe_3O_4 nanoparticles have received clinical approval from the Food and Drug Administration. The scaffolds loaded with Fe_3O_4 nanoparticles indeed effectively enhanced cell viability and promoted cell proliferation [46, 47]. However, the random arrangement of Fe_3O_4 nanoparticles in the scaffolds greatly compromised their positive magnetic stimulation effects, due to the mutual repulsive between adjacent magnetic dipoles.

In present study, we constructed Fe_3O_4@SiO_2 nanochains with uniform shell-core structure by magnetic-field-guided interface co-assembly of Fe_3O_4 nanoparticles (Fig. 2). The simulation analysis results of magnetic field distribution proved the orderly assembly of Fe_3O_4 nanoparticles in the Fe_3O_4@SiO_2 nanochains formed magnetic energy coupling and obtained a highly magnetic micro-field (Fig. 3a-c). The results are consistent with the analysis of Yin Yadong's team [48–50]. From the results of magnetic tests, the Fe_3O_4@SiO_2 nanochains

still preserved the superior superparamagnetism of Fe_3O_4 nanoparticles. The good magnetism and high surface areas endowed Fe_3O_4@SiO_2 nanochains with great potential for use in biomedicine.

To better understand the biological advantages of Fe_3O_4@SiO_2 nanochains in scaffolds, a series of in vitro cell experiments were performed. Compared to PLLA/Fe_3O_4 scaffolds, PLLA/Fe_3O_4@SiO_2 scaffolds are more conducive to cell adhesion and expansion, especially further enhancing cell viability, proliferation, differentiation, mineralization, and bone-related gene expressions (Figs. 5, 6 and 7). It could be attributed to the stronger magnetic stimulation effect of Fe_3O_4@SiO_2 nanochains. In terms of mechanism, the orderly assembly of Fe_3O_4 nanoparticles obtained magnetic energy coupling, resulting in a highly micro-field that stimulated the surrounding cells to respond (Fig. 8). In this case, the membrane flux of the diamagnetic cell membrane would be modified. Moreover, the strong magnetic singles would activate receptors on the cell membrane, thereby modulating a series of signaling pathways including Ca^{2+} channels, mitogen-activated protein kinase (MAPK), bone morphogenetic protein-2 (BMP-2) and integrins [6, 10, 41, 51]. Then, the corresponding downstream transcription factors were regulated, and consequently osteogenesis-related gene expressions of RUNX2, OPN, OCN and OSX were up-regulated. Hence, the Fe_3O_4@SiO_2 nanochains in scaffold possessed great potential in accelerating bone repair.

Conclusions

A magnetic-field-guided interface co-assembly of Fe_3O_4 nanoparticles had been demonstrated to rationally synthesis unique Fe_3O_4@SiO_2 nanochains. The obtained Fe_3O_4@SiO_2 nanochains exhibited high magnetic susceptibility and excellent magnetic induction intensity. Importantly, the superior magnetic properties of nanochains enhanced the interaction between PLLA/Fe_3O_4@SiO_2 scaffold and cells. As a result, the nanochains in scaffold effectively enhanced cell activity, proliferation, differentiation, and mineralization as well as bone-related gene expressions. These findings

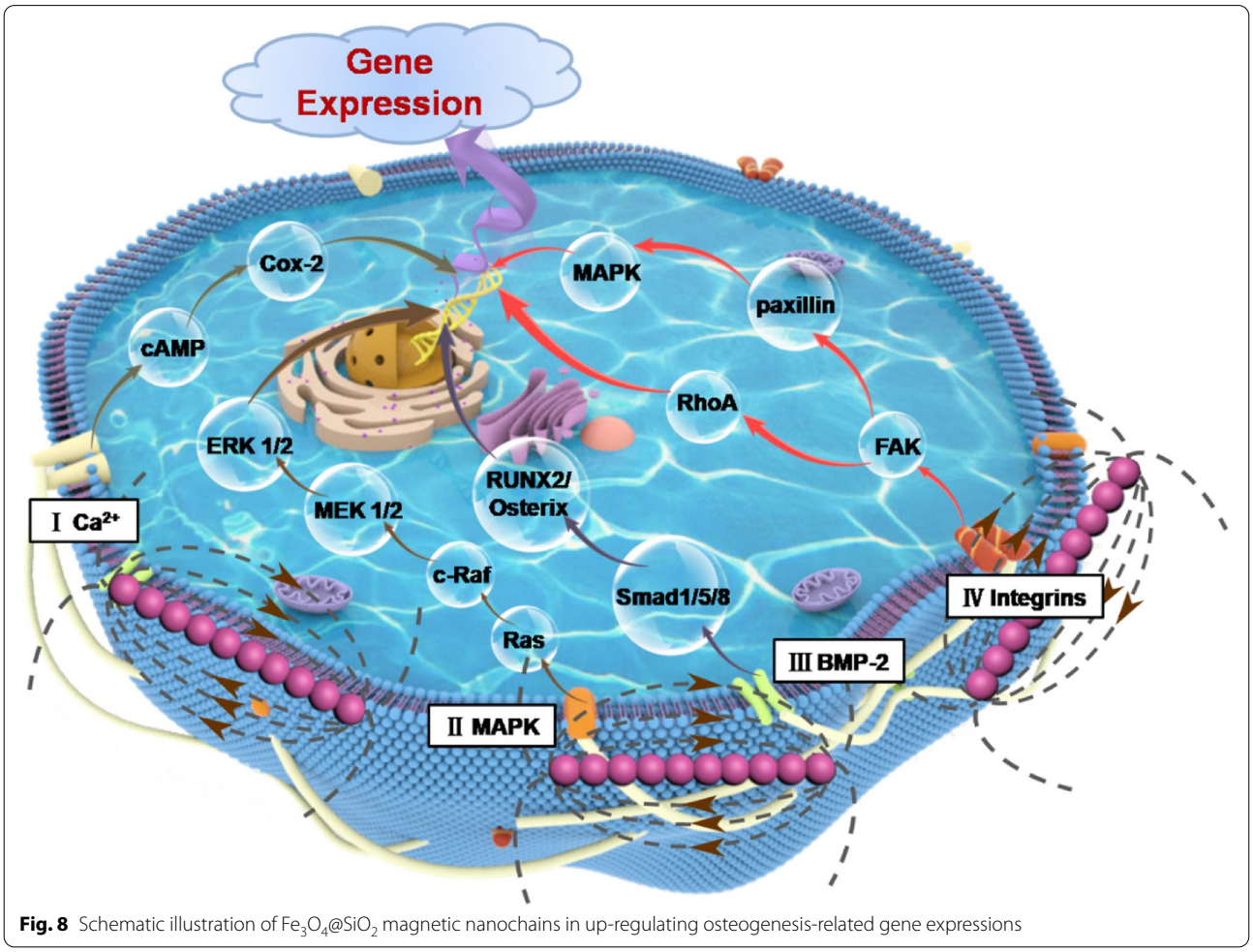

Fig. 8 Schematic illustration of Fe_3O_4@SiO_2 magnetic nanochains in up-regulating osteogenesis-related gene expressions

confirmed the superparamagnetic scaffold incorporated with Fe_3O_4@SiO_2 nanochains could accelerate the repair of bone defect.

Abbreviations
PLLA: Poly l-lactic acid; SiO_2: Silica; SLS: Selective laser sintering; TEOS: Tetraothorsilicate; TEM: Transmission electron microscope; XPS: X-ray photoelectron spectrometer; FTIR: Fourier transform infra-red spectrometer; XRD: X-ray diffractometer; VSM: Vibrating sample magnetometer; DMEM: Dulbecco's Modified Eagle's Medium; SEM: Scanning electron microscope; CCK-8: Cell Counting Kit-8; ALP: Alkaline phosphatase; Runx2: Runt-related transcription factor-2; OPN: Osteopontin; OCN: Osteocalcin; OSX: Osterix.

Acknowledgements
Not applicable.

Authors' contributions
Shuai CJ and Chen X contributed to acquisition, analysis of data, drafted and revised the manuscript. He CX and Qian GW contributed to analysis and interpretation of the data. Shuai Y and Peng SP contributed to performing the experiments. Deng YW and Yang WJ conceptualized the experimental research, acquired the financial support/experimental resources, validated the data and reviewed the paper. All authors read and approved the final manuscript.

Funding
This study was supported by the following funds: (1) The Natural Science Foundation of China (52105352, 51935014, 52165043, 82072084, 81871498); (2) The Project of Jiangxi University of Science and Technology (205200100535); (3) JiangXi Provincial Natural Science Foundation of China (2020ACB214004, 20202BAB214011); (4) The Provincial Key R&D Projects of Jiangxi (20201BBE51012); (5) The Project of State Key Laboratory of High Performance Complex Manufacturing.

Availability of data and materials
The datasets used and/or analysed during the current study are available from the corresponding author on reasonable request.

Declarations

Ethics approval and consent to participate
Not applicable.

Consent for publication
Not applicable.

Competing interests
The authors declare that they have no competing interests.

Author details
[1]Institute of Additive Manufacturing, Jiangxi University of Science and Technology, Nanchang 330013, China. [2]State Key Laboratory of High Performance Complex Manufacturing, Central South University, Changsha 410083, China. [3]College of Life Science and Technology, Huazhong University of Science and Technology, Wuhan 430074, China. [4]The Key Laboratory of Carcinogenesis and Cancer Invasion of the Chinese Ministry of Education, Xiangya Hospital, Central South University, Changsha 410078, China. [5]NHC Key Laboratory of Carcinogenesis of Hunan Cancer Hospital and the Affiliated Cancer Hospital of XiangyaSchool of MedicineSchool of Basic Medical Science, Cancer Research Institute, Central South University, Changsha 410013, China. [6]School of Energy and Machinery Engineering, Jiangxi University of Science and Technology, Nanchang 330013, China. [7]Department of Spine Surgery, Third Xiangya Hospital, Central South University, Changsha 410013, China.

Received: 15 March 2022 Accepted: 18 June 2022
Published online: 06 August 2022

References

1. Zhang M, Lin R, Wang X, Xue J, Deng C, Feng C, et al. 3D printing of Haversian bone-mimicking scaffolds for multicellular delivery in bone regeneration. Science Adv. 2020;6:eaa6725.
2. Othman Z, Fernandes H, Groot AJ, Luider TM, Alcinesio A, de Melo PD, et al. The role of ENPP1/PC-1 in osteoinduction by calcium phosphate ceramics. Biomaterials. 2019;210:12–24.
3. Pina S, Oliveira JM, Reis RL. Natural-based nanocomposites for bone tissue engineering and regenerative medicine: a review. Adv Mater. 2015;27:1143–69.
4. Qi F, Gao X, Shuai Y, Peng S, Deng Y, Yang S, et al. Magnetic-driven wireless electrical stimulation in a scaffold. Compos B Eng. 2022;237:109864.
5. Lew W-Z, Feng S-W, Lee S-Y, Huang H-M. The review of bioeffects of static magnetic fields on the oral tissue-derived cells and its application in regenerative medicine. Cells. 2021;10:2662.
6. Xia Y, Sun J, Zhao L, Zhang F, Liang X-J, Guo Y, et al. Magnetic field and nano-scaffolds with stem cells to enhance bone regeneration. Biomaterials. 2018;183:151–70.
7. Kong Y, Duan J, Liu F, Han L, Li G, Sun C, et al. Regulation of stem cell fate using nanostructure-mediated physical signals. Chem Soc Rev. 2021;50:12828–72.
8. Qiao Y, Liu X, Li B, Han Y, Zheng Y, Yeung KWK, et al. Treatment of MRSA-infected osteomyelitis using bacterial capturing, magnetically targeted composites with microwave-assisted bacterial killing. Nat Commun. 2020;11:1–13.
9. Khizar S, Ahmad NM, Zine N, Jaffrezic-Renault N, Errachid-el-salhi A, Elaissari A. Magnetic nanoparticles: From synthesis to Theranostic applications. ACS Applied Nano Materials. 2021;4(5):4284–306.
10. Shuai C, Yang W, He C, Peng S, Gao C, Yang Y, et al. A magnetic micro-environment in scaffolds for stimulating bone regeneration. Mater Des. 2020;185:108275.
11. Li J, Lu X, Zhang Y, Cheng F, Li Y, Wen X, et al. Transmittance tunable smart window based on magnetically responsive 1D nanochains. ACS Appl Mater Interfaces. 2020;12:31637–44.
12. Xiong Q, Lim CY, Ren J, Zhou J, Pu K, Chan-Park MB, et al. Magnetic nanochain integrated microfluidic biochips. Nat Commun. 2018;9:1–11.
13. Ma M, Zhang Q, Dou J, Zhang H, Yin D, Geng W, et al. Fabrication of one-dimensional Fe_3O_4/P (GMA-DVB) nanochains by magnetic-field-induced precipitation polymerization. J Colloid Interface Sci. 2012;374:339–44.
14. Ma M, Zhang Q, Zhang H, Xin T, Zhang B, Fan X. One-pot synthesis of highly magnetically sensitive nanochains coated with a fluorescent shell by magnetic-field-induced precipitation polymerization. Sci Adv Mater. 2013;5:623–9.
15. Sun J, Liu X, Huang J, Song L, Chen Z, Liu H, et al. Magnetic assembly-mediated enhancement of differentiation of mouse bone marrow cells cultured on magnetic colloidal assemblies. Sci Rep. 2014;4:1–8.
16. Zhou J, Wang C, Wang P, Messersmith PB, Duan H. Multifunctional magnetic nanochains: exploiting self-polymerization and versatile reactivity of mussel-inspired polydopamine. Chem Mater. 2015;27:3071–6.
17 Jia J, Yu JC, Wang Y-XJ, Chan KM. Magnetic nanochains of $FeNi_3$ prepared by a template-free microwave-hydrothermal method. ACS Appl Mat Interfaces. 2010;2:2579–84.
18. Li X, Sun L, Wang H, Xie K, Long Q, Lai X, et al. Synthesis of cobalt nanowires in aqueous solution under an external magnetic field. Beilstein J Nanotechnol. 2016;7:990–4.
19. Wan L, Song H, Chen X, Zhang Y, Yue Q, Pan P, et al. A magnetic-field guided interface coassembly approach to magnetic mesoporous silica nanochains for osteoclast-targeted inhibition and heterogeneous nanocatalysis. Adv Mater. 2018;30(25):1707515.
20 Qi F, Liao R, Shuai Y, Pan H, Qian G, Peng S, et al. A conductive network enhances nerve cell response. Addit Manufact. 2022;52:102694.
21. Shuai C, Wang Z, Peng S, Shuai Y, Chen Y, Zeng D, et al. Water-responsive shape memory thermoplastic polyurethane scaffold triggered at body temperature for bone defect repair. Mater Chem Front. 2022;6:1456–69.
22. Kralj S, Makovec D. Magnetic assembly of superparamagnetic iron oxide nanoparticle clusters into nanochains and nanobundles. ACS Nano. 2015;9:9700–7.
23. Kralj S, Potrc T, Kocbek P, Marchesan S, Makovec D. Design and fabrication of magnetically responsive nanocarriers for drug delivery. Curr Med Chem. 2017;24:454–69.

24. Tarhini M, Vega-Chacón J, Jafelicci M, Zine N, Errachid A, Fessi H, et al. Structured magnetic core/silica internal shell layer and protein out layer shell (BSA@SiO_2@SME): preparation and characterization. Chemistry Africa. 2020;3:127–34.
25. Bitar A, Vega-Chacón J, Lgourna Z, Fessi H, Jafelicci M Jr, Elaissari A. Submicron silica shell-magnetic core preparation and characterization. Colloids Surf, A. 2018;537:318–24.
26. Rajan A, Sharma M, Sahu NK. Assessing magnetic and inductive thermal properties of various surfactants functionalised Fe_3O_4 nanoparticles for hyperthermia. Sci Rep. 2020;10:1–15.
27. Wang L, Shen C, Cao Y. PVP modified Fe_3O_4@SiO_2 nanoparticles as a new adsorbent for hydrophobic substances. J Phys Chem Solids. 2019;133:28–34.
28. Chen Z, Wang H, Wang Y, Lv R, Yang X, Wang J, et al. Improved optical damage threshold graphene Oxide/SiO_2 absorber fabricated by sol-gel technique for mode-locked erbium-doped fiber lasers. Carbon. 2019;144:737–44.
29. Chen J, Qiao M, Wang W, Zhang Q. A novel magnetic mesoporous Fe_3O_4@Void@mSiO_2-Pd(0) nanochains with high heterogeneous catalysis efficiency for Suzuki coupling reaction. Compos Commun. 2019;16:41–9.
30. Feng P, Jia J, Peng S, Shuai Y, Pan H, Bai X, et al. Transcrystalline growth of PLLA on carbon fiber grafted with nano-SiO_2 towards boosting interfacial bonding in bone scaffold. Biomater Res. 2022;26:1–15.
31. Qi F, Wang Z, Shuai Y, Peng S, Shuai C. Sr^{2+} Sustained Release System Augments Bioactivity of Polymer Scaffold. ACS Appl Polymer Mater. 2022;4:2691–702.
32. Yang Y, Zan J, Shuai Y, Yang L, Zhang L, Zhang H, et al. In Situ growth of a metal-organic framework on graphene oxide for the chemo-photothermal therapy of bacterial infection in bone repair. ACS Appl Mater Interfaces. 2022;19:21996–2005.
33. Beltrán F, De La Orden M, Lorenzo V, Pérez E, Cerrada M, Urreaga JM. Water-induced structural changes in poly (lactic acid) and PLLA-clay nanocomposites. Polymer. 2016;107:211–22.
34. Yang L, Zou P, Cao J, Sun Y, Han D, Yang S, et al. Facile synthesis and paramagnetic properties of Fe_3O_4@SiO_2 core-shell nanoparticles. Superlattices Microstruct. 2014;76:205–12.
35. Augustine R, Dan P, Schlachet I, Rouxel D, Menu P, Sosnik A. Chitosan ascorbate hydrogel improves water uptake capacity and cell adhesion of electrospun poly (epsilon-caprolactone) membranes. Int J Pharm. 2019;559:420–6.
36. Yang M, Shuai Y, Yang Y, Zeng D, Peng S, Tian Z, et al. In situ grown rare earth lanthanum on carbon nanofibre for interfacial reinforcement in Zn implants. Virtual Phys Prototyp. 2022;17:1–18.
37. Deng F, Wu P, Qian G, Shuai Y, Zhang L, Peng S, et al. Silver-decorated black phosphorus: a synergistic antibacterial strategy. Nanotechnology. 2022;33:245708.
38. Shuai C, Yuan X, Shuai Y, Qian G, Yao J, Xu W, et al. Nitrogen-doped carbon-ZnO heterojunction derived from ZIF-8: a photocatalytic antibacterial strategy for scaffold. Mater Today Nano. 2022;18:1002105.
39. Bhattacharyya S, Ghosh SS. Transmembrane TNFα-expressed macrophage membrane-coated chitosan nanoparticles as cancer therapeutics. ACS Omega. 2020;5:1572–80.
40. Zhang Y, Liu S, Yao Y, Chen Y, Zhou S, Yang X, et al. Invasion and defense interactions between enzyme-active liquid coacervate protocells and living cells. Small. 2020;16:2002073.
41. Chen H, Sun J, Wang Z, Zhou Y, Lou Z, Chen B, et al. Magnetic cell-scaffold interface constructed by superparamagnetic IONP enhanced osteogenesis of adipose-derived stem cells. ACS Appl Mater Interfaces. 2018;10:44279–89.
42. Wang H, Zeng X, Pang L, Wang H, Lin B, Deng Z, et al. Integrative treatment of anti-tumor/bone repair by combination of MoS_2 nanosheets with 3D printed bioactive borosilicate glass scaffolds. Chem Eng J. 2020;396:125081.
43. Yang J, Zhang H, Shang P. Effect of static magnetic field on bone and its molecular mechanism. Chin Sci Bull. 2020;65:1238–50.
44. Xu H-Y, Gu N. Magnetic responsive scaffolds and magnetic fields in bone repair and regeneration. Front Mater Sci. 2014;8:20–31.
45. Zan J, Qian G, Deng F, Zhang J, Zeng Z, Peng S, et al. Dilemma and breakthrough of biodegradable poly-l-lactic acid in bone tissue repair. J Mater Res Technol. 2022;17(2369):2387.
46. Anjaneyulu U, Priyadarshini B, Vijayalakshmi U. Preparation of Ag doped hydroxyapatite-Fe_3O_4-chitosan composites: In vitro biocompatibility study on MG-63 cells for orthopedic applications. Adv Sci Lett. 2018;24:5901–6.
47. Wu ZC, Li WP, Luo CH, Su CH, Yeh CS. Rattle-Type Fe_3O_4@CuS Developed to Conduct Magnetically Guided Photoinduced Hyperthermia at First and Second NIR Biological Windows. Adv Func Mater. 2015;25:6527–37.
48. Li Z, Yang F, Yin Y. Smart materials by nanoscale magnetic assembly. Adv Func Mater. 2020;30:1903467.
49. Li Z, Wang M, Zhang X, Wang D, Xu W, Yin Y. Magnetic assembly of nanocubes for orientation-dependent photonic responses. Nano Lett. 2019;19:6673–80.
50. Wang M, He L, Yin Y. Magnetic field guided colloidal assembly. Mater Today. 2013;16:110–6.
51. Zhu Y, Yang Q, Yang M, Zhan X, Lan F, He J, et al. Protein corona of magnetic hydroxyapatite scaffold improves cell proliferation via activation of mitogen-activated protein kinase signaling pathway. ACS Nano. 2017;11:3690–704.

Publisher's Note